Research Article

Several Geological Issues of Schrödinger Basin Exposed by CE-2 CELMS Data

Z. G. Meng [iD],[1,2,3] **H. H. Wang,**[1] **Y. C. Zheng** [iD],[3] **Y. Z. Wang** [iD],[1] **H. Miyamoto,**[4]
Z. C. Cai,[2] **J. S. Ping,**[3] **and Y. Z. Zhu**[1]

[1]*College of Geoexploration Science and Technology, Jilin University, Changchun 130026, China*
[2]*State Key Laboratory of Lunar and Planetary Sciences, Macau University of Science and Technology, Macau*
[3]*Key Laboratory of Lunar and Deep Space Exploration, National Astronomical Observatories, Chinese Academy of Sciences,
 Beijing 100101, China*
[4]*The University Museum, University of Tokyo, Bunkyo-ku, Tokyo 113-0033, Japan*

Correspondence should be addressed to Y. C. Zheng; zyc@bao.ac.cn and Y. Z. Wang; iamwangyongzhi@126.com

The study on the Schrödinger basin may provide important clues about the formation of South Pole-Aitken (SPA) basin. In this paper, the thermophysical features of Schrödinger basin were evaluated using the Chang'E-2 microwave sounder (CELMS) data. The results are as follows. (1) The geological units are reevaluated with the CELMS data and a new geological view was provided according to the brightness temperature and emissivity maps. (2) The surface topography plays an important role in the observed CELMS data. (3) The hot anomaly in the basin floor indicates a warm substrate. (4) The pyroxene-bearing anorthosite is probably an important cause for the cold anomaly over the lunar surface. Also, the study proves the applicability of the CELMS data applying in high latitude regions to a certain extent.

1. Introduction

Schrödinger basin is the best preserved basin of its size and laid in the southwest corner of the South Pole-Aitken (SPA) basin (Figure 1(a)), the largest and oldest impact crater on the Moon [1, 2]. The basin is superposed on the floor of SPA basin and it may likely excavate the materials from the lower crust or upper mantle [2–4]. Thus, the diversity of the materials and the special mare volcanism in the basin could provide some important information about the formation of Schrödinger basin and even SPA basin.

Schrödinger basin, centered at (76°S, 134°E), is about 334 km in diameter. It also has an inner peak ring of 168 km in diameter represented by a discontinuous ring of mountains [5]. Wilhelms et al. [6] firstly provided the geological mapping effort of this basin at 1:5M scale based on Lunar Orbiter data. Thereafter, Shoemaker et al. [7] improved the geological interpretation with the Clementine UV-VIS data. Using the data from the Lunar Reconnaissance Orbiter, Clementine, Lunar Prospector, and Lunar

Orbiter, Mest [2] evaluated the contacts and structures of geological units and at last identified three groups including nine distinct units (Figure 1(b)), indicating that Schrödinger basin comprises the pre-Schrödinger crustal materials, the mafic and anorthositic materials, and the volcanic materials. Additionally, abundant fractures occur in the basin floor, some of which extend to a few hundred kilometers long. Shankar et al. [8] verified a heterogeneous distribution of both anorthositic and basaltic materials in the basin floor. Using remote sensing data and impact crater modeling, Kramer et al. [9] reevaluated the composition of materials that make up the basin wall, impact melt, and peak ring, providing a new understanding of basin-forming processes. Through analyzing the LRO LOLA data and the Chandrayaan data, Kumar et al. [10] concluded the boulder falls in the basin floor triggered by the recent shallow moonquakes and impact events, indicating that this is geologically active zone until now. Therefore, Schrödinger basin presents an appropriate place to evaluate the thermophysical features of the diverse materials forming the SPA and Schrödinger basins and the
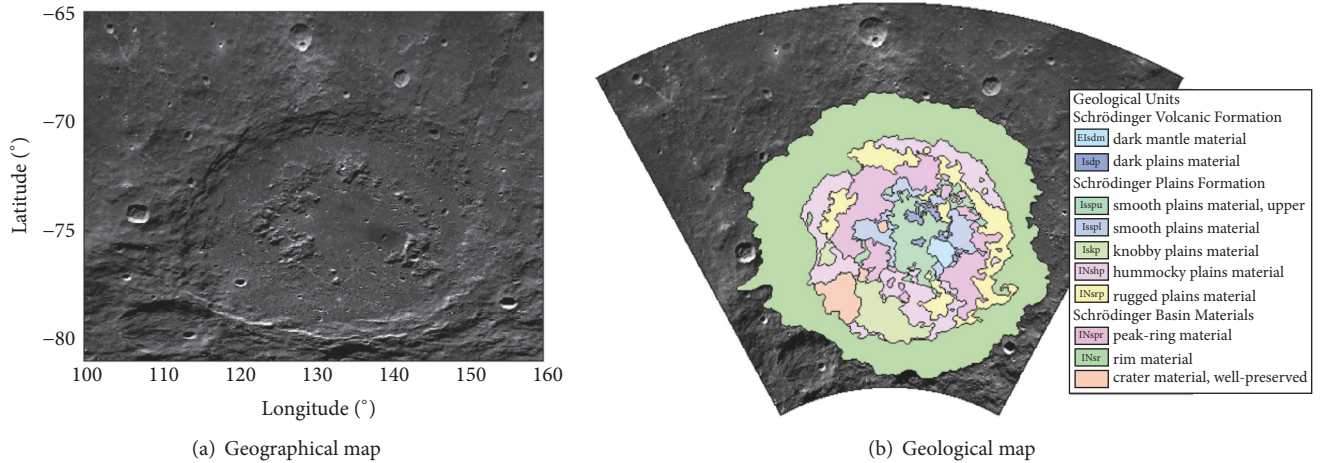
(a) Geographical map

(b) Geological map

Figure 1: WAC image (a) and geological map (b) of Schrödinger basin. Note: Figure 1(a) was downloaded from http://wms.lroc.asu.edu/lroc/search. Figure 1(b) geological map is interpreted by Mest [2].

substrate thermal features related to the tectonic activities. This is also the motivation for us to study the basin with the microwave sounder (CELMS) data.

The CELMS instrument was onboard Chinese Chang'E-2 (CE-2) satellite, which is designed to measure the thermal emission of the shallow lunar surface in microwave domain. The CELMS data are of special significance in the current lunar geological study, which has been proved by Meng et al. [11] and Hu et al. [12] through evaluating the mare volcanism in Mare Imbrium. Meng et al. [13] also gave a distinctly different view about Mare Crisium using the CE-2 CELMS data compared to the optical data and indicated a new understanding about the mare volcanism there. This hints to the potential applications of the CELMS data to better understand the thermal evolution of the Moon.

However, Schrödinger basin is located in high latitude regions, which has harsh topographic and illuminating conditions. To testify the applicability of the CELMS data in such conditions is also our motivation. In this paper, Section 2 thoroughly describes the processing of the CELMS data. Section 3 analyses the MTE features of the geological units in the basin. The geological applications are discussed in Section 4. Section 5 presents the conclusions.

2. Data Processing

Schrödinger basin is totally located in the high latitude region with fairly complex topographic and illuminating conditions, which makes it difficult to select and process the CELMS data [14–16].

2.1. CELMS Data Processing. The CELMS data used in the study were collected from the CE-2 satellite, which operated at 3.0, 7.8, 19.35, and 37 GHz channels. The observation time was from October 2010 to May 2011. The incident angle is $0°$, and the temperature sensitivity is better than 0.5 K. A detailed description of the CELMS data was given by Cai and Lan [17] and Meng et al. [18].

According to the range of Schrödinger basin, more than 600 tracks of swath CELMS data were acquired. For the brightness temperature (T_B) is heavily influenced by the surface temperature, or surface illumination [12, 16], the hour angle is introduced to describe the measured T_B in different time spans [11, 13, 15, 19, 20]. Additionally, the quantity of the selected CELMS data is more than five times as that with a similar area in low latitude regions [18]. However, after overlying the obtained CELMS data on Schrödinger basin (Figure 2), $1°$ spatial resolution along the latitude and very high spatial resolution along the longitude are clearly presented.

The soundly large quantity of the CELMS data means that the T_B maps at multiple time periods can be generated (Figure 3). But just as in Figure 3, we may obtain the CELMS data at 8 and 14 o'clock. Unfortunately, there occurs an apparent position problem in Figure 3, which is indicated by the red line. The position of the T_B in the left side of the red line apparently does not match that of the T_B in the right side, hinting that the CELMS data at this time are not proper. After carefully checking the original CELMS data, the CELMS data at 0 and 10 o'clock are proper to generate the T_B maps of Schrödinger basin, which can represent the T_B at nighttime and daytime.

Thereafter, the CELMS data processing procedure is similar to that suggested by Meng et al. [11]. For the linear interpolation method can slightly alter the original data, it is employed to generate the T_B maps with a spatial resolution of $0.25° \times 0.25°$ (Figure 4).

Figure 4 presents that the T_B distribution is strongly latitude-dependent. E.g., the T_B variation at 37 GHz with latitude from the north to the south is more than 100 K at daytime and about 90 K at midnight. But the T_B in the central basin floor is only about 10 K higher than its vicinity. That is, the T_B variation with the latitude is much larger than that resulted from the thermophysical parameters of the lunar regolith [13]. Therefore, this latitude-dependent impact must be eliminated before using the generated T_B maps.
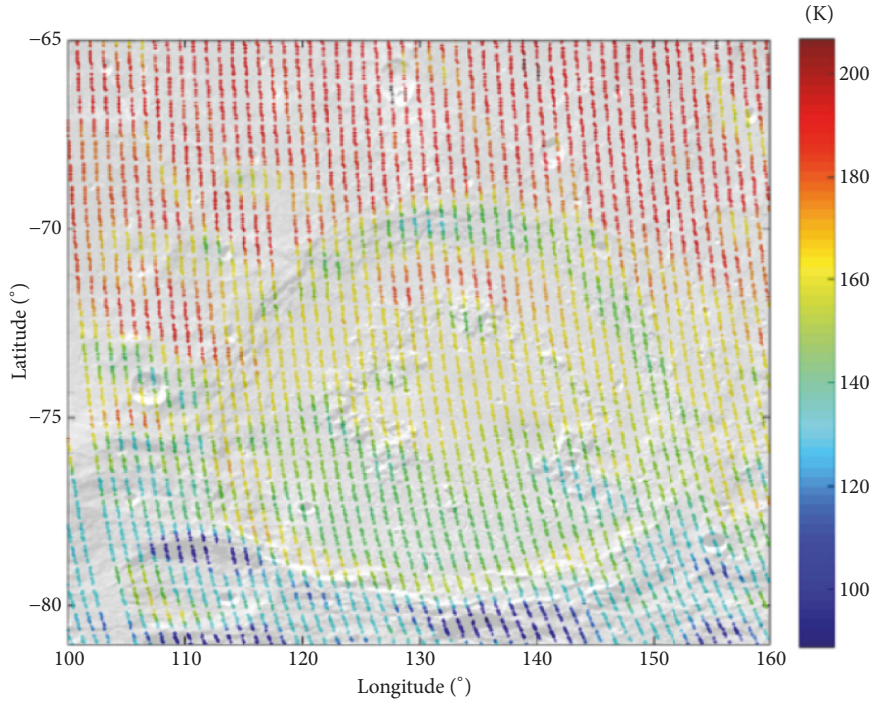
Figure 2: Scatter map of the 37-GHz CELMS data at noon overlays on WAC image.

Thus, the standard T_B of every latitude is proposed. Firstly, one T_B is selected for every latitude on the condition that the $(FeO+TiO_2)$ abundance, surface slope, and rock abundance are similar in all selected positions. Here, the selection criteria are same as Meng et al. [13]. The composition, surface slope, and rock abundance data are referred through JMARS software. The selected T_B for every channel is presented as a dash line in Figure 5. Thereafter, a fitting curve is made according to the selected T_B, which is defined as the standard TB for every latitude (Figure 5).

Finally, the normalized T_B (nT_B) can be calculated using the T_B divided by the standard T_B along the corresponding latitude. Figure 6 is the 37-GHz nT_B maps at 10 and 0 o'clock, which shows that the latitude-dependent effect of the T_B maps is well eliminated.

2.2. Image Cut and Overlaying. Figure 6 indicates a new different view about Schrödinger basin compared to the optical data, hinting at the potential geological applications of the CELMS data in high latitude regions. Largely, the nT_B behaviors show a good correlation with the topography, e.g., the northern interior wall with reduced solar illumination, and the composition, e.g., in the peak ring with relatively higher nT_B. However, the nT_B difference among the geological units is still not distinct. This mainly resulted from the nT_B values in Granswindt crater (111.2°E, 79.4°S) in the southwest and Nefed'ev crater (135.8°E, 81.1°S) in the south, whose nT_B is lowest in the selected regions, and from the southern interior wall of Grotrian crater (128.3°E, 66.2°S), whose nT_B is almost highest at daytime. Fortunately, the three mentioned regions are all situated beyond Schrödinger basin. Thus, to better understand the thermophysical features of the

geological units, only the nT_B within Schrödinger basin is kept, which is cut according to the boundary given by Mest [2] (Figures 7 and 8). Figures 7 and 8 show that the difference among the geological units is well strengthened compared to that in Figure 6.

What is more, the geological units have been fully studied by Mest [2] and Kramer et al. [9]. To improve the understanding of the geological meanings of the nT_B maps, the interpretation result by Mest [2] is vectorized and overlaid on the nT_B maps in black line. Also, the WAC image is overlaid by the 37-GHz-channel nT_B at daytime and midnight to postulate the detailed distribution of the nT_B values (Figure 9). The coincidence between the nT_B performances and the geological units as well as the topographic terrains is largely good, indicating the rationality of the generated nT_B maps.

2.3. Emissivity Maps Generation. In high latitude regions, the CELMS data will experience harsher solar illumination conditions compared to the low latitude regions [14, 15, 19]. This phenomenon is obviously indicated by the lowest values in the northern wall and by the highest values in the southern wall. Thus, how to eliminate the topographic impact is a crucial issue for the applications of the CELMS data.

Up to now, the surface temperature has been fully studied by means of the numerical simulation by Meng et al. [16], He et al. [21], and Hu et al. [22]. Therefore, the surface temperature was simulated with improved Racca model [16] using the CE-1 LAM data, which was recommended by Hu et al. [23] for its coincidence with the footprint of the CELMS data. For the parameters used, the reader can be referred to [16]. The original solar irradiance is the average
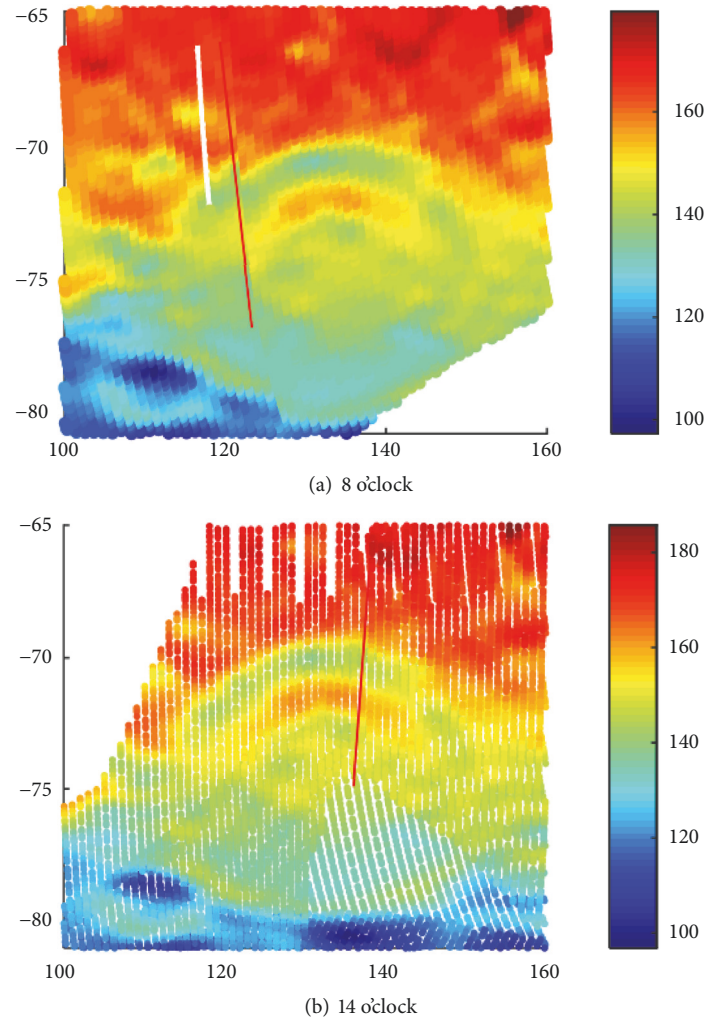
(a) 8 o'clock

(b) 14 o'clock

FIGURE 3: CELMS data at 8 (a) and 14 (b) o'clock (unit: K).

(a) 10 o'clock
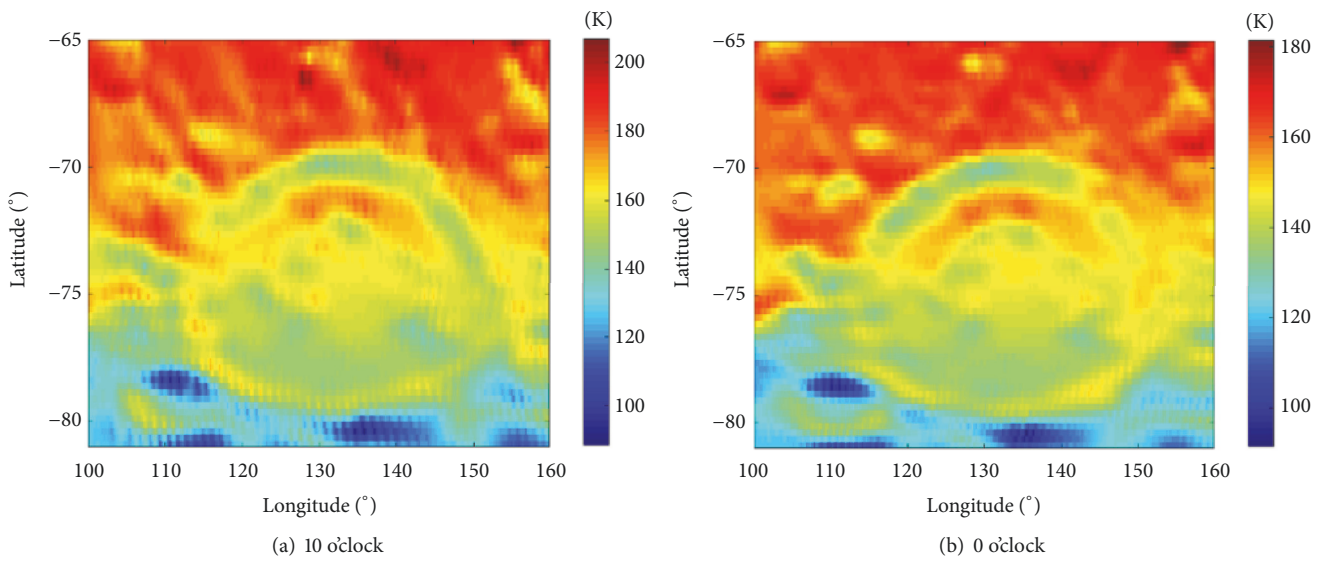
(b) 0 o'clock

FIGURE 4: T_B distribution map of Schrödinger basin at 37 GHz.
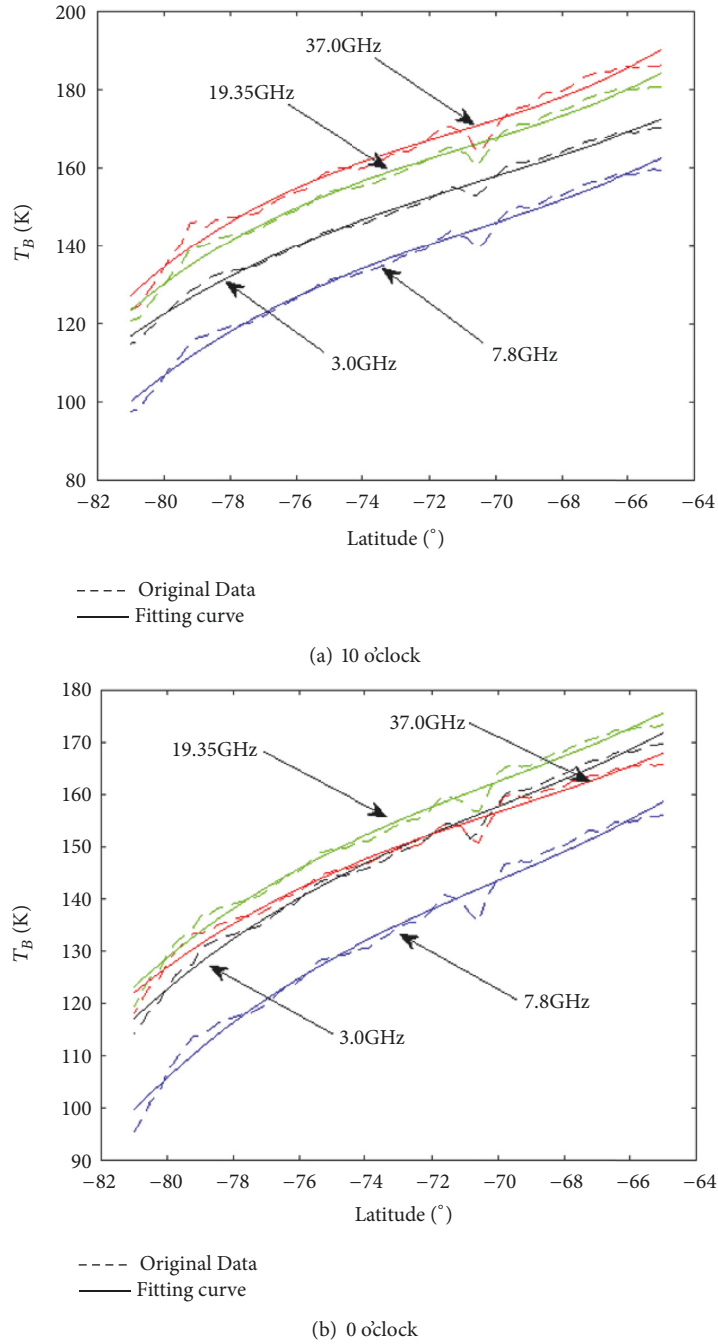
(a) 10 o'clock

(b) 0 o'clock

FIGURE 5: Generation of the standard T_B.

value. Moreover, the time used is at 10 o'clock, which is corresponding to the daytime CELMS data used in this study. Then, the ratio between the generated T_B and the surface temperature is the emissivity of the lunar regolith at the corresponding channel (Figure 10).

Compared to Figure 7, Figure 10 indicates that the influence from the surface topography is weakened to some extent, which can be expressed by the emissivity in the northern and southern interior walls. Thus, the emissivity map is also employed to provide supplements to improve understanding of the MTE features of the geological units.

However, the simulated surface temperature is in ideal conditions, which is not suitable for the real environment during the CELMS observation. Thus, the introduction of the surface temperature and the estimated emissivity are employed only for referring.

3. MTE Features of Schrödinger Basin

Mest [2] identified three groups in Schrödinger basin, including Schrödinger basin materials, Schrödinger plains
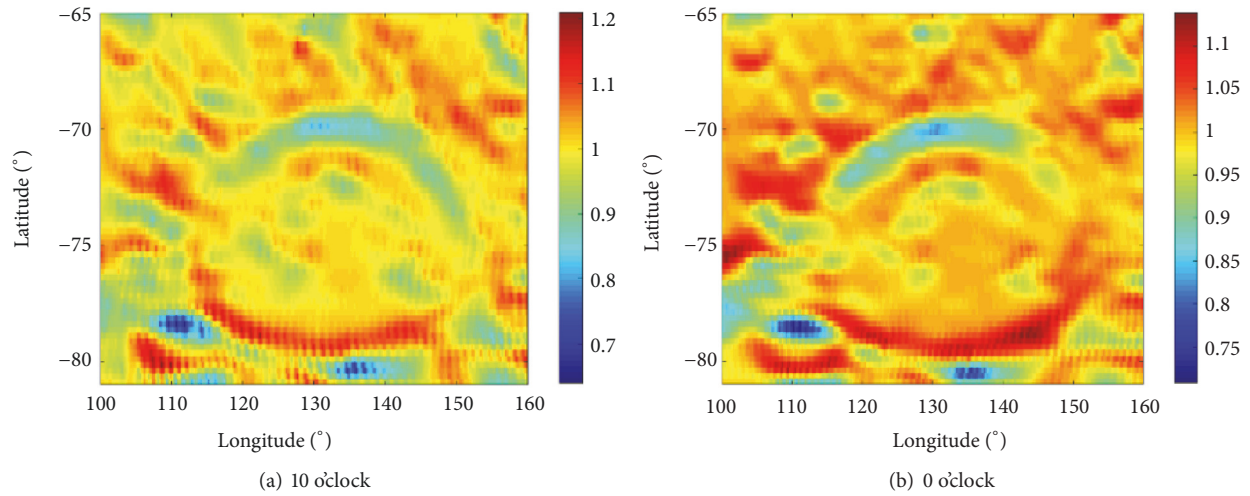
(a) 10 o'clock

(b) 0 o'clock

FIGURE 6: nT_B map of Schrödinger basin at 37 GHz.
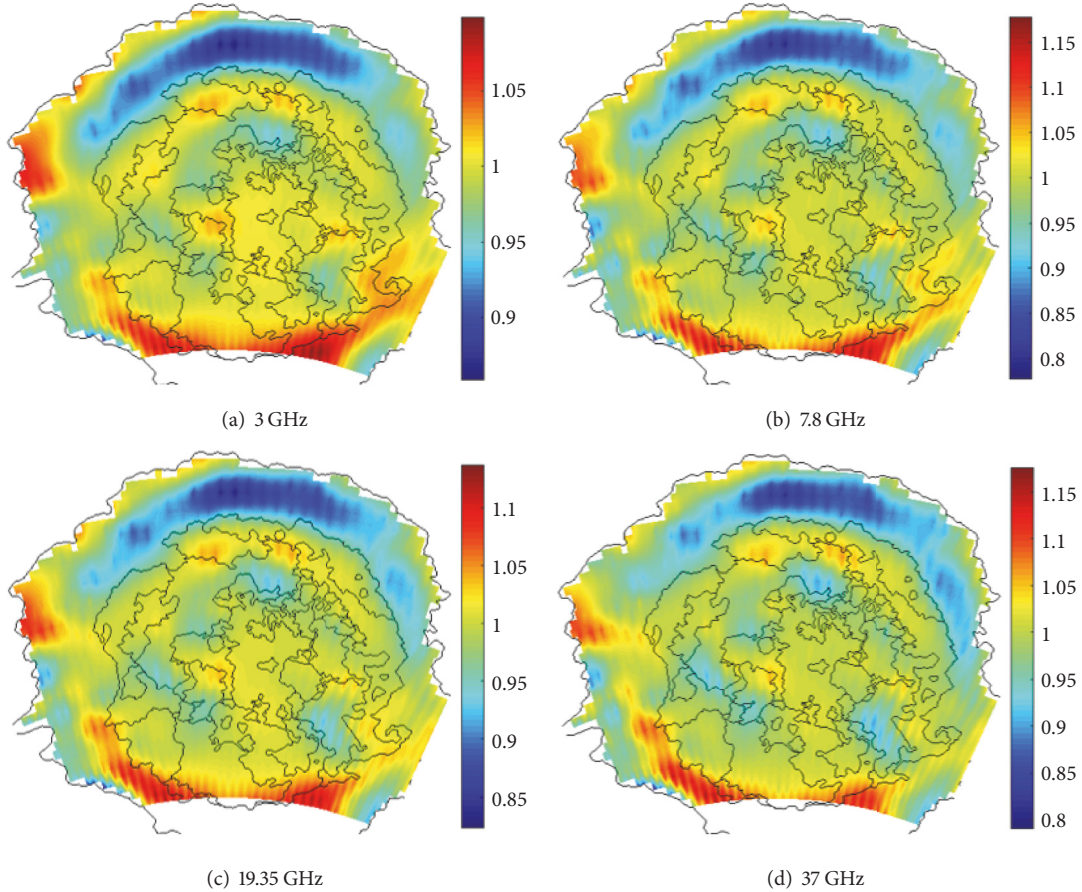

(a) 3 GHz

(b) 7.8 GHz

(c) 19.35 GHz

(d) 37 GHz

FIGURE 7: nT_B maps of the Schrödinger basin at 10 o'clock.

formation, and Schrödinger volcanic formation. Figures 7 and 8 indicate similar nT_B behaviors about Schrödinger basin. That is, though the T_B at daytime is higher than that at nighttime, the region with relatively higher nT_B at daytime also shows relatively higher values at nighttime and vice versa.

This presents special microwave thermal emission (MTE) features about the materials in the basin.

3.1. Schrödinger Basin Materials Group. Schrödinger basin materials comprise the peak-ring unit (INspr) and basin rim
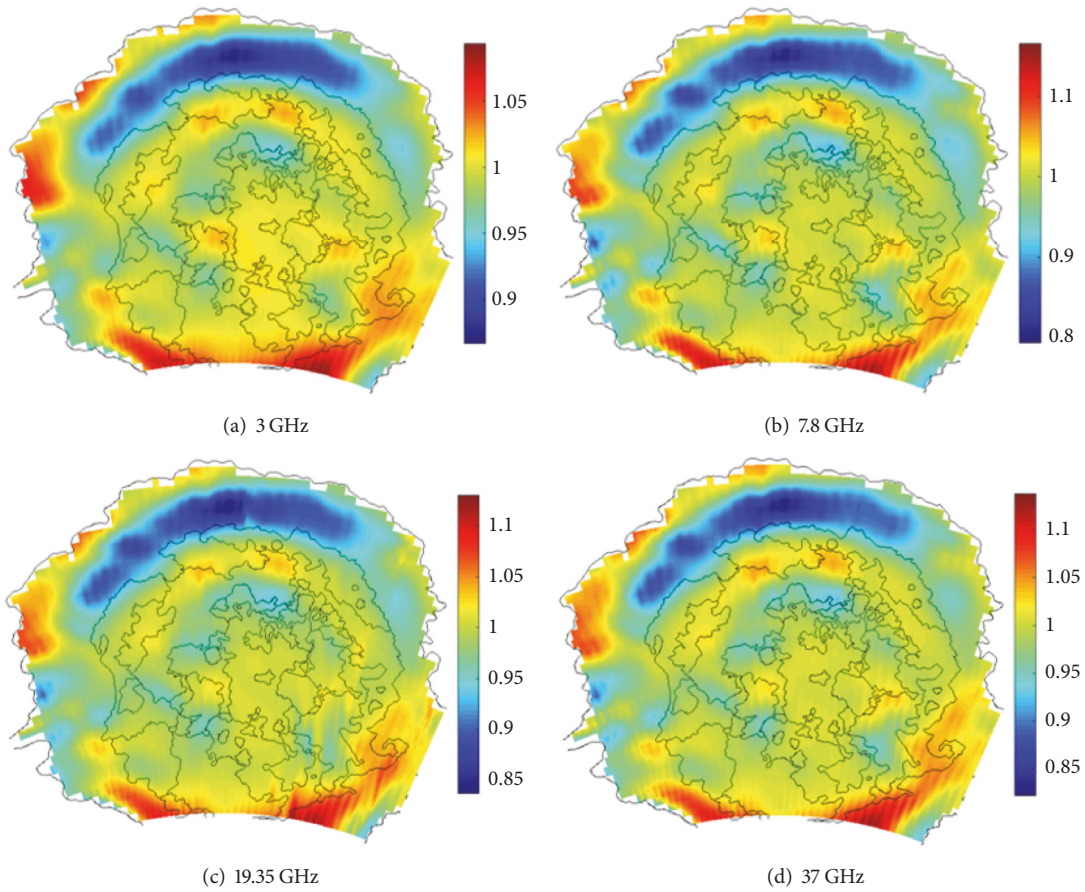
(a) 3 GHz

(b) 7.8 GHz

(c) 19.35 GHz

(d) 37 GHz

FIGURE 8: nT_B maps of the Schrödinger basin at 0 o'clock.
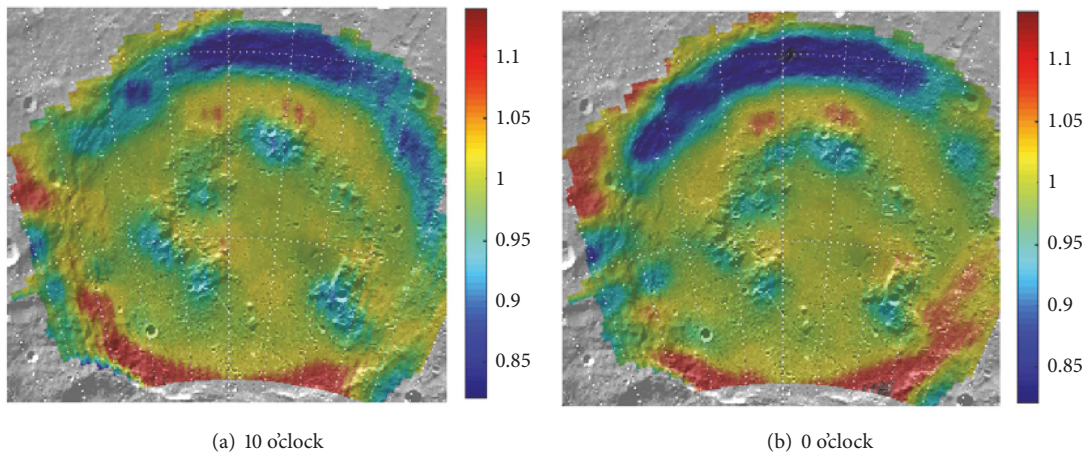

(a) 10 o'clock

(b) 0 o'clock

FIGURE 9: 37-GHz nT_B map overlays on WAC image with 60% transparency.

unit (INsr) (Figure 1(b)), which is interpreted to consist of pre-Schrödinger crustal materials [2].

Unit INspr is the incomplete peak ring of mountainous terrain, which displays moderate albedo in Clementine images but is mottled in high-resolution LROC images [2]. Figures 7 and 8 indicate that the unit has rather low nT_B values at daytime and midnight, especially at 3.0 GHz maps.

The regions with low nT_B apparently form an incomplete ring, coinciding well with its terrain. But, several regions around (127.3°E, 72.3°S), (129.0°E, 75.3°S), (134.4°E, 71.6°S), and (143.0°E, 75.2°S) present the relatively higher nT_B than their vicinities. Combined with the topography map, such regions are slopes originating to the solar illumination, indicating the strong influence of the topography on the
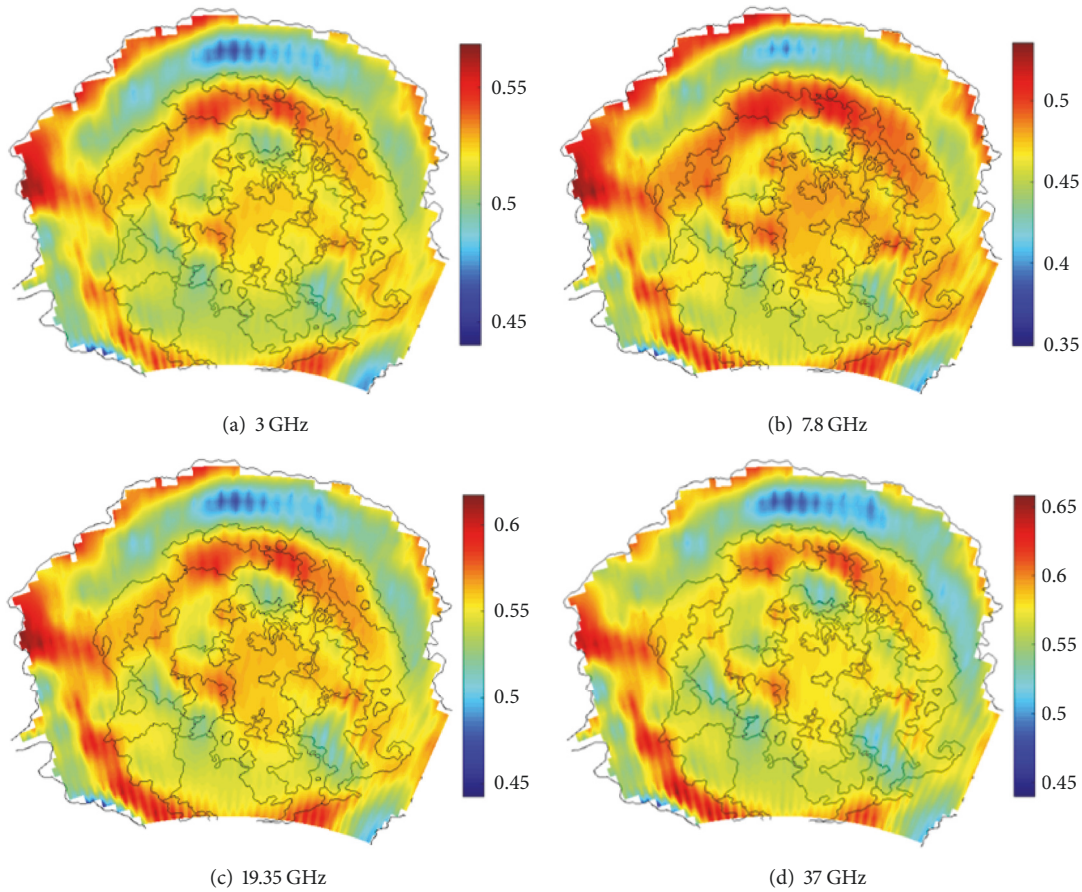
(a) 3 GHz

(b) 7.8 GHz

(c) 19.35 GHz

(d) 37 GHz

FIGURE 10: Emissivity maps of Schrödinger basin.

nT_B. Even so, much more regions of the unit show considerably low nT_B values, implying that the material of the unit can be represented by the low MTE feature. Zheng et al. [15] and Meng et al. [24] proposed that the low MTE is directly related to the low (FeO +TiO$_2$) abundance (FTA). This means that the material of the unit will be severely low in FTA. Figure 10 indicates that the unit has a low emissivity, indicating a high density of the material in this unit combined with the relationships expressed by [25].

Unit INsr includes the materials that form the topographic rim crest and the interior wall of Schrödinger basin. But the nT_B in the unit is heavily impacted by the surface topography. At daytime, the nT_B in the north interior wall is lowest within the study area, while the south interior wall indicates the highest nT_B. A similar phenomenon occurs in the nighttime nT_B maps. Such phenomenon also exists in Tycho crater [26, 27], indicating the cold and hot T_B anomalies over the lunar surface. This makes it difficult to recognize the MTE features of the material in this unit.

3.2. Schrödinger Plains Group. The floor of Schrödinger basin is identified as five plains-forming units, including the rugged plains material (INsrp), hummocky plains material (INshp), the lower member of the smooth plains material (Isspl), the upper member of the smooth plains material (Isspu), and the knobby plains material (Iskp) [2].

Unit INsrp is mainly distributed outside of the peak ring, which is stratigraphically the oldest plains material on the basin floor. The unit shows relatively higher nT_B in the northern, western, and southern parts, while the nT_B changes greatly from north portion to the south and with frequency. The great change of the nT_B performance makes it difficult to recognize the MTE features of the material in this unit.

Unit INshp occupies much of the basin floor along the northern and western walls, and in the south where the peak ring is most discontinuous. The nT_B and emissivity performances of the unit are similar to that of unit Insrp in the close areas, indicating the uniformity of the materials MTE features in the two units.

Unit Isspu primarily occurs in the center of Schrödinger basin, which presents as lower and slightly less cratered than unit Isspl. Interestingly, the unit has the second highest nT_B within the basin floor, which is just lower than the regions with enhanced solar illumination. This indicates that the unit can be represented by the high MTE feature and the material here is fairly high in FTA. Figure 10 indicates that the emissivity is high here, indicating a relatively lower density of the material in this unit.

Unit Isspl is found just inside the peak ring, displaying moderate to high albedo with a small number of superposed craters. Interestingly, nearly in all boundaries between this unit and unit INspr, the nT_B and emissivity differences are not clear. A similar phenomenon also occurs in the boundaries between this unit and unit Isspu. Generally, Figure 10 indicates that the emissivity in most part of the unit is similar to that in unit Isspu, implying the uniformity of the densities of the materials in two units.

Unit Iskp is located along the southern basin wall with fairly high albedo. The nT_B distribution of the unit is obviously affected by the surface topography, which is higher in the southern portion near the south interior wall but lower in the northern portion. Even so, the nT_B is lower than the nearby regions along the same latitude, indicating that the unit should be represented by the low MTE feature. Moreover, the nT_B and emissivity performances of the unit are similar to that of unit Inspr in the close areas, indicating the uniformity of the materials MTE features in the two units.

3.3. Schrödinger Volcanic Formation. Volcanic materials are concentrated in the northern and eastern parts of the basin inside the peak ring. The formation is made up of four patches of dark plains materials unit (Isdp) and dark mantle material unit (Elsdm) [2].

The largest patch of unit Isdp is mainly located along the northern part of the peak ring, and other three patches of this unit are located around unit EIsdm. The unit displays smooth, relatively featureless, low-albedo surfaces. But, not only at nT_B maps but also at emissivity map is the difference between this unit and unit Isspu not clear, indicating the uniformity of the materials MTE features in the two units.

Unit Elsdm is located in the southeastern part of the basin floor within the peak ring, which has a relatively smooth, lightly cratered surface with low albedo. There exists an ovoidal cone, which has been identified as the source of pyroclastic eruptions [7, 28]. In nT_B and emissivity maps, the values in this unit are apparently lower than the nearby unit Isspu, particularly at 3.0 GHz channel, while the nT_B values are apparently higher than those in unit INspr. This not only indicates the difference of the materials MTE features in these regions, but also hints at the applicability of the CELMS data in the high latitude regions.

4. Geological Applications

Figures 7 and 8 postulate a new view about the geological units in Schrödinger basin.

4.1. Potential Geological Applications. The nT_B behaviors present a distinctly different view about Schrödinger basin compared to the visible images.

To basin materials formation, unit INspr indicates the low nT_B and emissivity values, hinting the existence of the materials with high density.

To plains formation, the difference between units INsrp and INshp is not clear both in nT_B maps and in emissivity maps. Though the nT_B and emissivity values change greatly
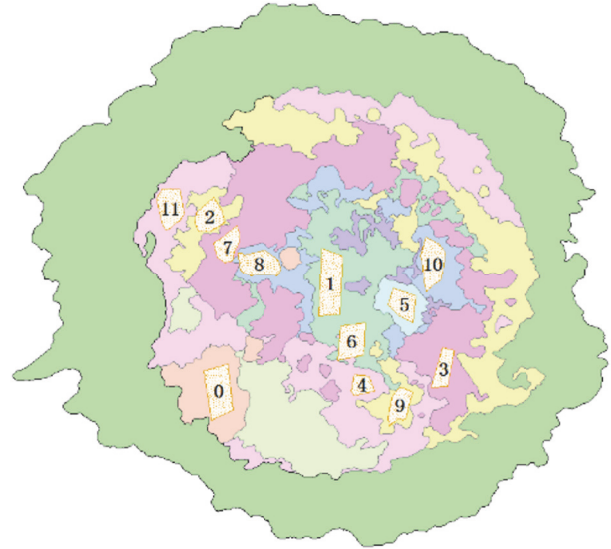

FIGURE 11: Samples for statistics.

from the south to north part of the basin, they show identical features in the close regions. This means the uniformity of the materials in the two units.

Also, the difference between units Isspl and Isspu is not clear, indicating the uniformity of the materials in the microwave range. Additionally, the nT_B and emissivity performances make it difficult to identify the MTE features of units INsrp and INshp, but the emissivity values in unit Isspl are apparently higher than those in unit Insrp in the southern part of the basin floor, indicating that the materials in units Isspl and Isspu are different from units INsrp and INshp.

To volcanic formation, unit Isdp is hard to identify from the unit Isspu in the nT_B and emissivity maps. That is, units Isdp and Isspl indicate the similar nT_B and emissivity performances as unit Isspu, indicating the uniformity of the materials in the three units in microwave range.

Here, unit Elsdm indicates the special nT_B and emissivity performances compared to the other units. The material here is identified as the dark mantle deposit or pyroclastic deposit [2, 29]. Thus, the nT_B and emissivity maps indicate the special thermophysical features of the deposits in high latitude regions.

To better understand the previous expression, the special regions mentioned above are sampled in Figure 11 and the corresponding statistics are presented in Table 1.

Table 1 indicates a small difference in nT_B values among the geological units, indicating some interesting information about the geological units as follows. First, unit INsrp represented by Positions 2 and 9 has the highest nT_B values. Interestingly, unit INshp represented by Positions 4, 6, and 11 has similar statistics to unit INsrp. Second, unit Isspu represented by Position 1 is lower than that in unit INsrp. Third, unit Elsdm represented by Position 5 has the third highest nT_B values. Fourth, unit INspr represented by Positions 3 and 7 apparently has the lowest nT_B values. Finally, the change of the nT_B with frequency in unit Isspl represented by Position

TABLE 1: nT_B statistics of samples at daytime.

Frequency	3 GHz		7.8 GHz		19.35 GHz		37 GHz	
Position	Mean	Std	Mean	Std	Mean	Std	Mean	Std
2	1.0071	0.0020	1.0124	0.0041	1.0177	0.0025	1.0147	0.0034
4	1.0041	0.0008	1.0068	0.0012	1.0082	0.0012	1.0105	0.0017
6	1.0092	0.0010	1.0119	0.0019	1.0120	0.0014	1.0141	0.0020
9	1.0001	0.0054	0.9994	0.0063	0.9997	0.0072	1.0003	0.0074
11	1.0023	0.0095	1.0025	0.0122	1.0013	0.0090	1.0061	0.0069
1	1.0064	0.0016	1.0076	0.0018	1.0078	0.0024	1.0086	0.0036
5	0.9989	0.0018	0.9960	0.0044	0.9973	0.0031	0.9965	0.0046
0	0.9759	0.0027	0.9545	0.0063	0.9596	0.0030	0.9498	0.0034
3	0.9719	0.0066	0.9518	0.0149	0.9542	0.0120	0.9410	0.0172
7	0.9762	0.0055	0.9511	0.0101	0.9555	0.0065	0.9421	0.0080
8	0.9712	0.0069	0.9609	0.0114	0.9630	0.0089	0.9447	0.0120
10	0.9562	0.0060	0.9651	0.0105	0.9640	0.0082	0.9517	0.0102

8 is similar to that of unit INsrp, indicating the difference in material MTE features. Combined with the emissivity map, unit Isspl is consistent with unit Isspu.

Therefore, a new geological understanding about Schrödinger basin can be obtained based on nT_B and emissivity maps and statistics of sample regions (Table 1). Here, at least in microwave range, the basin floor can be categorized into four geological zones. The first zone comprises the previous units INsrp and INshp. The second zone comprises the previous units INspr and Iskp. The third zone includes the previous units Isspl, Isspu, and Isdp. And the fourth zone is unit Eldsm.

The new geological understanding also means that though the surface features are not identical for the nearby geological unit, the MTE parameters of the materials are consistent. However, the strong topographic effect and the rather small nT_B differences among the geological units hint that the CELMS data are not suitable to study the regolith thermophysical features and the mare volcanism in high latitude regions.

4.2. nT_B Anomalies. At least four nT_B anomalies occur in Schrödinger basin. Two anomalies are hot, which mainly include the southern interior wall and the central part of the basin floor. The other two are cold, including the northern interior wall and unit INspr.

Hot and cold T_B anomalies are always an interesting topic in the current lunar study [12, 15, 19, 27, 30, 31], but the causes for the cold anomaly have long been in intense debate. Gong and Jin [32] and Hu et al. [12] attributed the hot and cold T_B anomaly to the existence of the rocks. But Salisbury and Hunt [33] and Meng et al. [27] thought that the surface topography and its orientation are the decisive factors for T_B anomaly. The nT_B behaviors in Schrödinger basin apparently prove the latter explanation, because the cold nT_B anomaly in the northern interior wall obviously resulted from the deficiency of the solar heating in a day, while the hot anomaly in the southern interior wall is apparently brought by the enhanced solar heating. Moreover, combined with the simulation results, the hot anomaly in the regions

around (127.3°E, 72.3°S), (129.0°E, 75.3°S), (134.4°E, 71.6°S), and (143.0°E, 75.2°S) also validates the strong influence of the solar heating on the anomaly of this kind.

However, there also exists another kind of hot and cold anomaly.

Firstly, in the central and southern parts of the basin floor, the nT_B is high no matter at daytime and at midnight, indicating a hot anomaly here. A similar phenomenon also exists in the basin floors of Orientale, Hertzsprung, and Crisium [13, 18, 20]. Using the theoretical model and the CE-2 CELMS data, Meng et al. [13, 20] attributed the hot T_B anomaly to the probably warm substrate.

However, to verify the conclusion, the influence of the surface topography and regolith composition must be eliminated at first. Interestingly, the emissivity maps and the topography both indicate a relatively flat surface in this region, indicating the negligible impact of the topography. Moreover, Meng et al. [24] and Hu et al. [12] suggested the strong influence of the ilmenite content on the local T_B. Similar findings are also proved by the observed CELMS data in Mare Imbrium and Orientale, where the mare basalts with higher ilmenite content indicate a higher T_B at daytime [11, 20]. The regolith in these regions is more mafic than the nearby regions [2], but the nT_B behaviors are opposed to the simulation results by Meng et al. [24] and Hu et al. [12] and observations in Mare Imbrium and Orientale [11, 20]. Thus, the regolith composition also cannot interpret the hot anomaly.

Again, the only left cause for the hot nT_B anomaly is the warm substrate.

Additionally, Lu et al. [34] found two apparent mascons in the central and south parts of Schrödinger basin. The formation of the mascons is always related to the volcanic activity in lower crust or upper mantle [35, 36]. Thus, the existence of the two mascons hints at an ever-existing strong volcanic activity in the deep lunar crust in Schrödinger basin. What is more, there occur abundant fractures in the basin floor, some of which have been proved to be related to the volcanic activity in depth [10]. This is a new evidence of the ever-existed strong tectonic activities in Schrödinger basin.

The hot anomaly, the abundant fractures, and the occurrence of the mascons indicate a new view about the volcanic activity in Schrödinger basin. This may provide some interesting information about the formation of the SPA basin and the mare volcanism of the lunar farside, deserved to be further studied with more sources of data in future.

Secondly, in unit INspr, the nT_B is always lower than the nearby units, while the solar illumination here is not apparently lower than the nearby regions, indicating the existence of a cold anomaly here. The causes for the low nT_B anomaly are still under debate until now.

First, the cold anomaly is obviously not related to the surface topography, for it is widely distributed in the peak ring. Some regions of the peak ring are originating to the solar illumination, while the nT_B here is still rather low.

Second, Gong and Jin [32] and Hu et al. [12] suggested that the rock abundance is responsible for the cold anomaly at night using the theoretical model. They also suggested that the cold anomaly at night should be a hot anomaly at noon. But the nT_B here is low both at daytime and at night, indicating that the rock abundance does not interpret the cold anomaly.

Third, Hu et al. [12] thought the ilmenite content is one of the main causes for the T_B anomalies found in the CELMS map. Also, Meng et al. [13] evaluated the relationship between the nT_B performances in the cold anomalies surrounding Mare Crisium and the corresponding rock abundance and ilmenite content, and the results also hint that a special material with rather low ilmenite should also be responsible for the cold anomaly. Furthermore, the T_B behaviors around Copernicus crater verified that the cold anomaly is likely brought by a special material with rather low ilmenite content [37].

That is, the composition should undertake the main cause for the low nT_B anomaly.

Therefore, the existence of the cold nT_B anomaly in unit INspr indicates that the source material, pyroxene-bearing anorthosite [28], is probably an important cause for the cold anomaly of the lunar surface, which also deserved to be further studied in future.

One more phenomenon should be paid attention to. Such cold anomaly is not only limited in unit INspr. The crater ejecta in the southwest part of the basin floor and just inside the peak ring also shows low nT_B and emissivity values as unit INspr, even if the regions are close to the southern interior wall. Additionally, the nT_B and emissivity in unit Iskp are apparently lower than the vicinity along the same latitude, indicating that the material in this unit should be represented by low values. The nT_B and emissivity in the northern part of unit Iskp are also similar to unit INspr. The crater ejecta represents the materials from the depth layer. Therefore, combined with the previous discussions, this phenomenon means that the materials in the depth layer of the basin floor excavated by the crater are similar to the peak ring. This is helpful to better understand the formation of Schrödinger basin and even the SPA basin according to the crater formation mechanism, which deserves to be further studied with more sources of data and even in situ observations.

5. Conclusions

In this paper, the nT_B maps derived from CE-2 CELMS data were systematically used to study the microwave thermophysical features of Schrödinger basin, which give some different aspects compared to the previous understandings. The main results are as follows.

(1) The geological units are reevaluated with the CE-2 CELMS data and the statistics of typical regions, which shows a different geological perspective compared to the visible results.

(2) The nT_B anomalies in the interior basin wall indicate the strong influence of the topography and its orientation.

(3) The hot nT_B anomaly in the basin floor indicates the likely warm substrate. Combined with the existence of the mascons and abundant floor fractures, the strong tectonic activity should ever exist in Schrödinger basin, which will be helpful to improve understanding the formation of the Schrödinger basin and even the SPA basin.

(4) The cold nT_B anomaly in unit INspr indicates that the pyroxene-bearing anorthosite is probably an important cause for the cold anomaly over the lunar surface.

Generally, the CELMS data are feasible to study the thermophysical features of the geological units in high latitude regions to some extent, which will expand our knowledge about the south and north poles. However, the surface topography strongly alters the T_B and nT_B performances, and more work should be done to further understand the important findings in this study.

Data Availability

The CELMS data can be downloaded from the website http://www.clep.org.cn/. The processed CELMS data and the brightness temperature maps about Schrödinger basin can be freely shared by email.

Conflicts of Interest

The authors declare that there are no conflicts of interest regarding the publication of this paper.
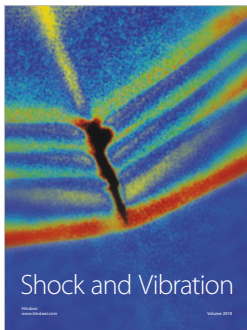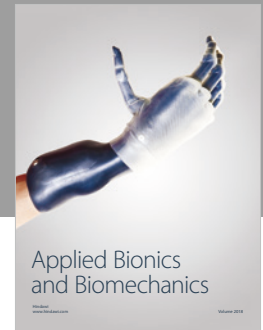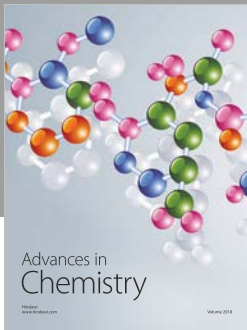
Acknowledgments

References

[1] P. D. Spudis, "Early crustal evolution. book reviews: the geology of multi-ring impact basins. the moon and other planets," *Science*, vol. 264, pp. 1180-1181, 1994.

[2] S. C. Mest, "The geology of Schrödinger basin: insights from post-Lunar Orbiter data," *Geological Society of America*, vol. 477, pp. 95–115, 2011.

[3] I. Garrick-Bethell and M. T. Zuber, "Elliptical structure of the lunar South Pole-Aitken basin," *Icarus*, vol. 204, no. 2, pp. 399–408, 2009.

[4] K. Uemoto, M. Ohtake, J. Haruyama et al., "Purest anorthosite distribution in the lunar South Pole-Aitken basin derived from SELENE multiband imager," in *Proceedings of the 41st Lunar and Planetary Science Conference*, 2010.

[5] D. A. Kring, G. Y. Kramer, and P. W. K. Potter, "Interpreting the depth of origin of the Schrödinger peak ring and implications for other impact basins," Lpi Contributions, 2013.

[6] D. E. Wilhelms, K. A. Howard, and H. G. Wilshire, "USGS Map I-1162 US Geological Survey," Washington, DC, USA, 1979.

[7] E. M. Shoemaker, M. S. Robinson, and E. M. Eliason, "The south pole region of the moon as seen by Clementine," *Science*, vol. 266, no. 5192, pp. 1851–1854, 1994.

[8] B. Shankar, G. R. Osinski, I. Antonenko, and C. D. Neish, "A multispectral geological study of the schrödinger impact basin," *Canadian Journal of Earth Sciences*, vol. 50, no. 1, pp. 44–63, 2013.

[9] G. Y. Kramer, D. A. Kring, A. L. Nahm, and C. M. Pieters, "Spectral and photogeologic mapping of Schrödinger Basin and implications for post-South Pole-Aitken impact deep subsurface stratigraphy," *Icarus*, vol. 223, no. 1, pp. 131–148, 2013.

[10] P. S. Kumar, U. Sruthi, N. Krishna et al., "Recent shallow moonquake and impact-triggered boulder falls on the Moon: New insights from the Schrödinger basin," *Journal of Geophysical Research Planets*, vol. 121, no. 2, pp. 147–179, 2016.

[11] Z. Meng, S. Hu, T. Wang, C. Li, Z. Cai, and J. Ping, "Passive microwave probing mare basalts in mare imbrium using CE-2 CELMS data," *IEEE Journal of Selected Topics in Applied Earth Observations and Remote Sensing*, vol. 11, no. 9, pp. 3097–3104, 2018.

[12] G. P. Hu, R. Bugiolacchi, K. L. Chan, Y. C. Zheng, and K. T. Tsang, "A new map of thermal variations within Oceanus Procellarum and Mare Imbrium using Chang'e (CE-2) microwave radiometers (MRMs) data," in *Proceedings of the 49th Lunar and Planetary Science Conference*, 2018.

[13] Z. G. Meng, H. H. Wang, X. Y. Li et al., "Potential geological significations of Crisium basin revealed by CE-2 CELMS data," *International Archives of the Photogrammetry, Remote Sensing and Spatial Information Sciences*, vol. 42, no. XLII-3, pp. 1279–1284, 2018.

[14] W. G. Zhang, J. S. Jiang, H. G. Liu et al., "Distribution and anomaly of microwave emission at Lunar South Pole," *Science China Earth Sciences*, vol. 53, no. 3, pp. 465–474, 2010.

[15] Y. C. Zheng, K. T. Tsang, K. L. Chan et al., "First microwave map of the Moon with Chang'E-1 data: the role of local time in global imaging," *Icarus*, vol. 219, no. 1, pp. 194–210, 2012.

[16] Z. G. Meng, Y. Xu, Z. C. Cai, S. B. Chen, Y. Lian, and H. Huang, "Influence of lunar topography on simulated surface temperature," *Advances in Space Research*, vol. 54, no. 10, pp. 2131–2139, 2014.

[17] Z. Cai, T. Lan, and C. Zheng, "Hierarchical MK splines: algorithm and applications to data fitting," *IEEE Transactions on Multimedia*, vol. 19, no. 5, pp. 921–934, 2017.

[18] Z. Meng, Q. Wang, H. Wang, T. Wang, and Z. Cai, "Potential geologic significances of hertzsprung basin revealed by CE-2 CELMS data," *IEEE Journal of Selected Topics in Applied Earth Observations and Remote Sensing*, vol. 11, no. 10, pp. 3713–3720, 2018.

[19] K. L. Chan, K. T. Tsang, B. Kong, and Y.-C. Zheng, "Lunar regolith thermal behavior revealed by Chang'E-1 microwave brightness temperature data," *Earth and Planetary Science Letters*, vol. 295, no. 1-2, pp. 287–291, 2010.

[20] Z. Meng, J. Zhang, Z. Cai, J. Ping, and Z.-S. Tang, "Microwave thermal emission features of mare orientale revealed by CELMS data," *IEEE Journal of Selected Topics in Applied Earth Observations and Remote Sensing*, vol. 10, no. 6, pp. 2991–2998, 2017.

[21] L. He, L. Lang, Q. Li, and W. Zheng, "Effect of surface roughness on microwave brightness temperature from lunar surface: numerical analysis with a hybrid method," *Advances in Space Research*, vol. 51, no. 1, pp. 179–187, 2013.

[22] G. P. Hu, Y. C. Zheng, A. A. Xu, and Z. S. Tang, "Lunar surface temperature of global moon: preparation of database with topographic and albedo effects," *IEEE Geoscience and Remote Sensing Letters*, vol. 13, no. 1, pp. 110–114, 2016.

[23] G. P. Hu, Y. C. Zheng, A. A. Xu, and Z. S. Tang, "Qualitative verification of CE-2's microwave measurement: relative calibration based on brightness temperature model and data fusion," *IEEE Transactions on Geoscience and Remote Sensing*, vol. 54, no. 3, pp. 1598–1609, 2016.

[24] Z. G. Meng, G. D. Yang, J. S. Ping et al., "Influence of (FeO+TiO2) abundance on the microwave thermal emissions of lunar regolith," *Science China Earth Sciences*, vol. 59, no. 7, pp. 1498–1507, 2016.

[25] G. H. Heiken, D. T. Vaniman, and B. M. French, *A User's Guide to the Moon*, Cambridge Univ. Press, London, UK, 1991.

[26] R. W. Shorthill and J. M. Saari, "Nonuniform cooling of the eclipsed moon: a listing of thirty prominent anomalies," *Science*, vol. 150, no. 3693, pp. 210–212, 1965.

[27] Z. G. Meng, R. Zhao, Z. C. Cai et al., "Microwave thermal emission at Tycho area and its geological significance," *IEEE Journal of Selected Topics in Applied Earth Observations and Remote Sensing*, vol. 10, no. 6, pp. 1–7, 2017.

[28] L. R. Gaddis, M. I. Staid, J. A. Tyburczy, B. R. Hawke, and N. E. Petro, "Compositional analyses of lunar pyroclastic deposits," *Icarus*, vol. 161, no. 2, pp. 262–280, 2003.

[29] D. A. Kring, G. Y. Kramer, G. S. Collins, R. W. K. Potter, and M. Chandnani, "Peak-ring structure and kinematics from a multidisciplinary study of the Schrödinger impact basin," *Nature Communications*, Article ID 13161, 2016.

[30] Z. G. Meng, L. Cui, T. X. Wang, Z. C. Cai, and J. S. Ping, "Cold behavior of moon surface demonstrated by typical copernican craters using CE-2 CELMS data," in *Proceedings of the International Geoscience and Remote Sensing Symposium*, IEEE, July 2018.

[31] B. C. Murray and R. L. Wildey, "Surface temperature variations during the lunar nighttime," *The Astrophysical Journal*, vol. 139, no. 5, pp. 734–750, 1964.

[32] X. H. Gong and Y. Q. Jin, "Diurnal change of thermal emission with 'hot spots' and 'cold spots' of fresh lunar craters observed by Chinese Chang'E-1," *Scientia Sinica*, vol. 42, no. 8, p. 923, 2012.

[33] J. W. Salisbury and G. R. Hunt, "Infrared images of Tycho on dark moon," *Science*, vol. 155, no. 3766, pp. 1098–1100, 1967.

[34] Y. Lu, J. S. Ping, and V. V. Shevchenko, "Volcanic activity of the Mare Moscoviense and Schrödinger basin," in *Proceedings of the Lunar and Planetary Science Conference*, 2013.

[35] P. D. Spudis, B. Bussey, J. Plescia, J.-L. Joset, and S. Beauvivre, "Geology of shackleton crater and the south pole of the moon," *Geophysical Research Letters*, vol. 35, no. 14, pp. 63–72, 2008.

[36] A. J. Dombard, S. A. Hauck II, and J. A. Balcerski, "On the origin of mascon basins on the Moon (and beyond)," *Geophysical Research Letters*, vol. 40, no. 1, pp. 28–32, 2013.

[37] Z. G. Meng, X. Y. Li, S. B. Chen et al., "Thermophysical features of shallow lunar crust demonstrated by typical Copernican craters using CE-2 CELMS data," *IEEE Journal of Selected Topics in Applied Earth Observations and Remote Sensing*, vol. 99, pp. 1–10, 2019.